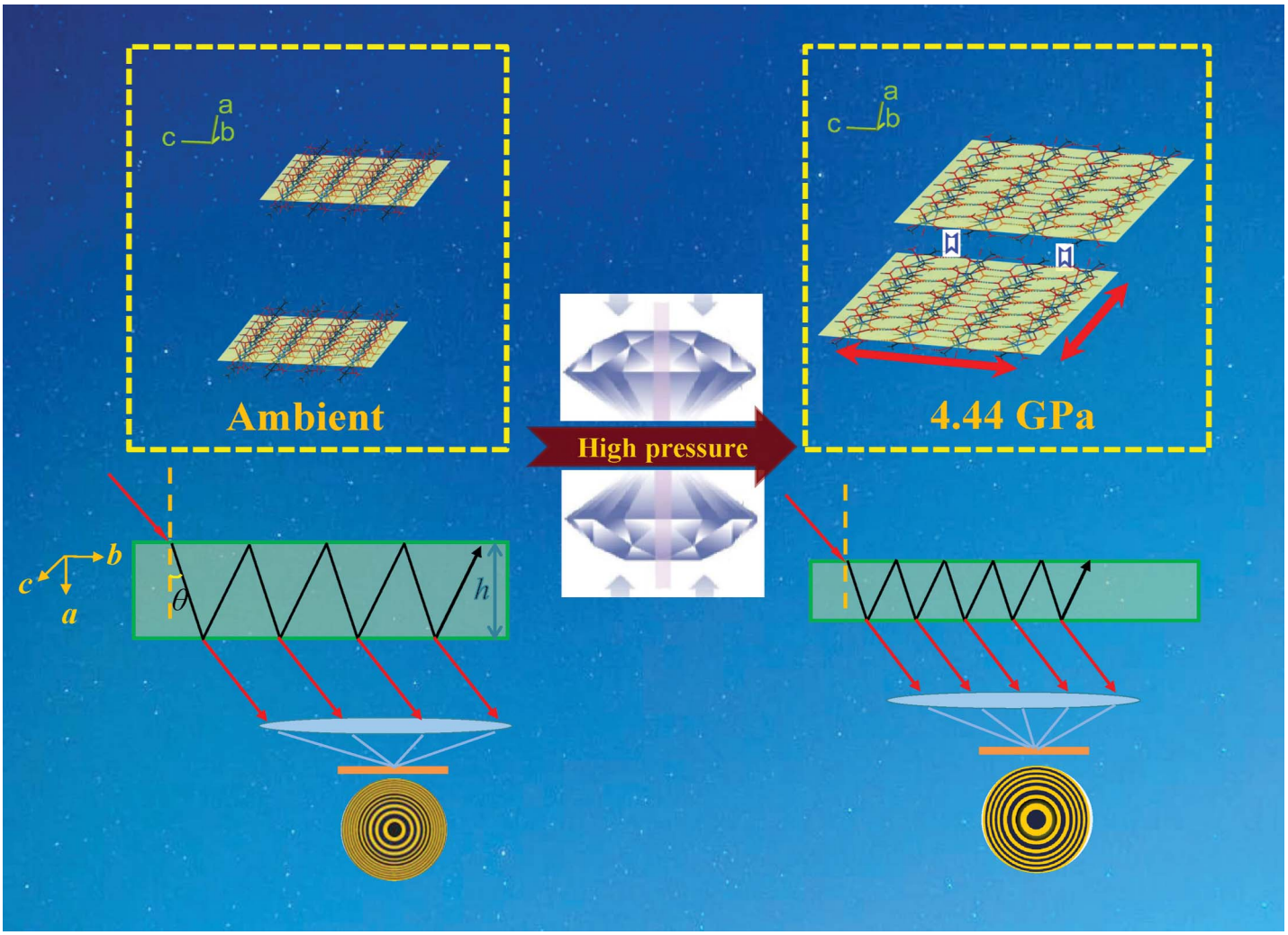


**Showcasing research from Professor Wei Li's laboratory, School of Materials Science and Engineering, Nankai University, Tianjin, China.**

Negative area compressibility of a hydrogen-bonded two-dimensional material

Very few materials expand two-dimensionally under pressure, and such an extremely rare phenomenon is termed as negative area compressibility (NAC). Here, large NAC has been discovered in a hydrogen-bonded 2D supramolecular coordination complex, $Zn(CH_3COO)_2 \cdot 2H_2O$. Mechanistic studies reveal that the significant NAC, over a wide pressure range of 0.15-4.44 GPa, stems from the complex cooperation of in-plane coordination and hydrogen-bonding interactions, and out-of-plane Van der Waals forces. Such NAC crystals could have potential applications as pressure-converting materials in ultrasensitive pressure sensing devices.

## As featured in:


See Wei Li, Weizhao Cai, Zheshuai Lin, Peixiang Lu *et al.*, *Chem. Sci.*, 2019, **10**, 1309.

ROYAL SOCIETY OF CHEMISTRY | Celebrating IYPT 2019

rsc.li/chemical-science

Registered charity number: 207890

Chemical Science

EDGE ARTICLE

View Article Online
View Journal | View Issue



Cite this: *Chem. Sci.*, 2019, **10**, 1309

All publication charges for this article have been paid for by the Royal Society of Chemistry

# Negative area compressibility of a hydrogen-bonded two-dimensional material†

Guoqiang Feng,[abc] Wei-Xiong Zhang,[d] Liyuan Dong,[c] Wei Li,*[ac] Weizhao Cai,*[e] Wenjuan Wei,[c] Lijun Ji,[c] Zheshuai Lin*[f] and Peixiang Lu*[cg]

Received 25th July 2018
Accepted 2nd December 2018

DOI: 10.1039/c8sc03291b

rsc.li/chemical-science

Very few materials expand two-dimensionally under pressure, and this extremely rare phenomenon, namely negative area compressibility (NAC), is highly desirable for technological applications in pressure sensors and actuators. Hitherto, the few known NAC materials have dominantly been limited to 2D crystals bonded *via* coordination interactions while other 2D systems have not been explored yet. Here, we report the large NAC of a hydrogen-bonded 2D supramolecular coordination complex, $Zn(CH_3COO)_2{\cdot}2H_2O$, with a synergistic microscopic mechanism. Our findings reveal that such an unusual phenomenon, over a wide pressure range of 0.15–4.44 GPa without the occurrence of any phase transitions, arises from the complex cooperation of intra-layer coordination and hydrogen-bonding interactions, and inter-layer van der Waals forces. In addition, we propose that these NAC crystals could have important applications as pressure-converting materials in ultrasensitive pressure sensing devices.



## Introduction

Materials that possess large mechanical anisotropy to external pressure are highly desirable due to their potential for technological application in next-generation microscale or nanoscale pressure sensors and actuators.[1,2] Recently, new classes of materials, such as coordination polymers,[3–7] metal–organic frameworks (MOFs)[8–10] and molecular crystals,[11,12] were found to show negative linear compressibility (NLC) properties, *i.e.* they expand along one direction when compressed uniformly.[13] This counterintuitive behaviour is generally associated with the wine-rack-like geometric motif: horizontal expansion couples with shrinkage in the vertical direction during framework hinging. It is well known that all materials must fulfil the thermodynamic requirement: their intrinsic volumes should decrease under hydrostatic compression. Hence, the most extreme and counterintuitive response to pressure is negative area compressibility (NAC): an expansion of a plane is perpendicular to the direction of strongest contraction. The uncommon NAC effect is extremely rare, and only very few compounds have been experimentally observed.[14–17] For example, the recently reported porous MOF $[Zn(L)_2(OH)_2]_n{\cdot}H_2O$, where L is 4-(1*H*-naphtho[2,3-*d*]imidazole-1-yl)benzoate with tetragonal symmetry, shows the strongest NAC response so far, its giant piezomechanical response arising from cooperation of the flexible $[–Zn–O(H)–]_n$ coordination helices and puckered $[–Zn–L–]_4$ quadrangular rings.[17]

Recently, two dimensional (2D) materials have been found to show remarkable physical properties under pressure which include structural reorganization,[18] semiconductor-to-metal transition,[19] enhanced tunneling magnetoresistance[20] and superconductivity.[21] More interestingly, NAC phenomena have also been found in 2D materials. For example, the layered silver(I) tricyanomethanide framework, which has orthorhombic symmetry, exhibits weak NAC along the *ac* plane below 0.62 GPa due to the flattening of puckered honeycomb-like layers.[15] This mechanism has also been found to be the driving force for a few inorganic NAC materials, such as KBBF,[22] $TlGaSe_2$ (ref. 23) and $NaV_2O_5$.[14] Despite the emerging interest in the NAC effects on the aforementioned 2D materials bonded *via* coordination interactions, hydrogen-bonded 2D systems have not attracted much attention. As hydrogen-bonding is fundamentally different from coordination bonds in terms of electronic nature,[24] this virgin field could widen the territory of NAC

[a]School of Materials Science and Engineering, Nankai University, Tianjin 300350, China. E-mail: wl276@nankai.edu.cn
[b]Department of Physics and Mechanical & Electrical Engineering, Hubei University of Education, Wuhan 430205, China
[c]School of Physics, Huazhong University of Science and Technology, Wuhan 430074, China. E-mail: lupeixiang@hust.edu.cn
[d]School of Chemistry and Chemical Engineering, Sun Yat-Sen University, Guangzhou 510275, China
[e]Department of Physics and Astronomy, University of Utah, Salt Lake City, Utah 84112, USA. E-mail: wzhcai@gmail.com
[f]Center for Crystal R&D, Key Lab of Functional Crystals and Laser Technology of Chinese Academy of Sciences, Technical Institute of Physics and Chemistry, Chinese Academy of Sciences, Beijing 100190, China. E-mail: zslin@mail.ipc.ac.cn
[g]Laboratory for Optical Information Technology, Wuhan Institute of Technology, Wuhan 430205, China

† Electronic supplementary information (ESI) available. See DOI: 10.1039/c8sc03291b

materials. To explore this possibility, here we report the discovery of the large negative area compressibility (NAC) phenomenon over a wide pressure range up to 4.44 GPa in zinc acetate dihydrate ($Zn(CH_3COO)_2\cdot 2H_2O$), a commonly used food supplement and drug for treating cold.[25] Our high-pressure synchrotron powder X-ray diffraction (HP-PXRD) experiments and first-principles calculations reveal that the intrinsic NAC in $Zn(CH_3COO)_2\cdot 2H_2O$ arises from the concerted opposite-rotating of the 'fan-shaped' $[Zn(CH_3COO)\cdot H_2O]^+$ coordination unit.

## Results and discussion

$Zn(CH_3COO)_2\cdot 2H_2O$ is a coordination complex and crystallizes in the monoclinic system with space group $C2/c$ as shown in Fig. S1.† Within the complex, the Zn atom is coordinated by two water molecules and four O atoms of two acetate ligands to form a distorted octahedral geometry. The adjacent zinc complexes are linked through O–H···O hydrogen bonds with distances of 2.608 and 2.638 Å along the *b* and *c* axes to generate a layered supramolecular architecture (Fig. 1a and S1†).[26] The neighboring layers are stacked down the *a*-axis with a skewed angle of 76°, *via* van der Waals interactions with an interlayer spacing of 7.090 Å. As expected for a 2D material, (100) is the major face of the formed crystals.

Considering the 2D nature of this molecular material, we characterized the crystals using transmission electron microscopy (TEM) and atomic force microscopy (AFM). The bulk crystals were ground gently in ethanol, and then the resulting suspension was deposited on a holey carbon support film prior to TEM testing. Bright-field images show nanosheets having good morphology with lateral sizes of about 200–800 nm (Fig. 1b). Moreover, the thickness of the nanosheets was quantified using AFM. As shown in Fig. 1c, the AFM image of a typical multi-layered nanosheet exhibits a thickness of about 4–5 nm (Fig. 1d), which corresponds to the height of ~7 layers. The ease of exfoliation indicates the significant mechanical anisotropy in the crystal structure of $Zn(CH_3COO)_2\cdot 2H_2O$, which has been further probed *via* a single-crystal nano-indentation experiment.[27] The (100) and (001) faces were indented with a Berkovich tip with a radius of ~50 nm in the quasi-static mode and the load-indentation depth (*P*–*h*) curves are displayed in Fig. S2.† There are several discrete displacement bursts ('pop-ins') in the loading portion on both faces, which indicate the fragile nature of hydrogen-bonding and layered packing motif in $Zn(CH_3COO)_2\cdot 2H_2O$, similar to other molecular crystals.[28] The average values of the elastic modulus ($E$) are 5.8(3) and 4.3(2) GPa for the (001) and (100) planes, respectively, giving an anisotropy ratio ($E_{(001)}/E_{(100)}$) of 1.35.

To explore the pressure effect on the structure of $Zn(CH_3COO)_2\cdot 2H_2O$, we carried out high-pressure powder X-ray diffraction (HP-PXRD) experiments in diamond anvil cells at room temperature.[29] Fig. 2a and b show the evolution of the relative lattice parameters with respect to the pressure from ambient pressure to 4.44 GPa (Table S1†). It is apparent that no phase-transition was detected in the whole measured pressure range and the crystal retains its monoclinic symmetry (Fig. S3–S5†). Both the unit-cell volume ($V$) and lattice parameter *a* undergo pronounced reductions of about 18% and 20% up to 4.44 GPa, while the *c*-axis and β angle decrease only by about 1.9% and 7.1%, respectively. However, the *b*-axis expands by about 2.3%, giving anomalous negative linear compressibility behavior. This abnormal behavior can be clearly evidenced by the (001) Bragg peak's shift to the low diffraction angle region (high *d*-spacing) under compression (Fig. S5†). As $Zn(CH_3COO)_2\cdot 2H_2O$ crystallizes in the monoclinic space group $C2/c$, its

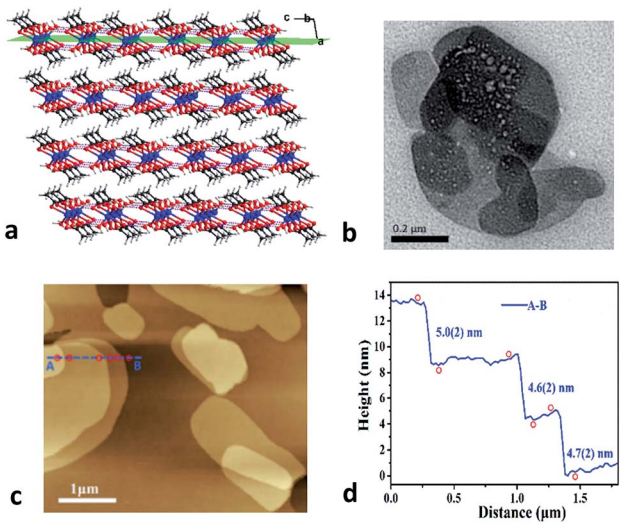


Fig. 1 (a) Supramolecular structure of $Zn(CH_3COO)_2\cdot 2H_2O$, showing the stacking of hydrogen-bonded layers (lying in the *bc*-plane) along the *a*-axis. Note: the green plane represents an individual hydrogen-bonded layer. Colour scheme: Zn, blue; O, red; C, black; H, white; the purple dotted lines represent the O–H···O hydrogen bonds. (b) Bright-field TEM image obtained at 293 K for $Zn(CH_3COO)_2\cdot 2H_2O$ nanosheets. Note: the tiny holes in the observed nanosheets represent damage caused by the strong electron beam. (c) and (d) Typical AFM image and height profile of $Zn(CH_3COO)_2\cdot 2H_2O$ nanosheets.

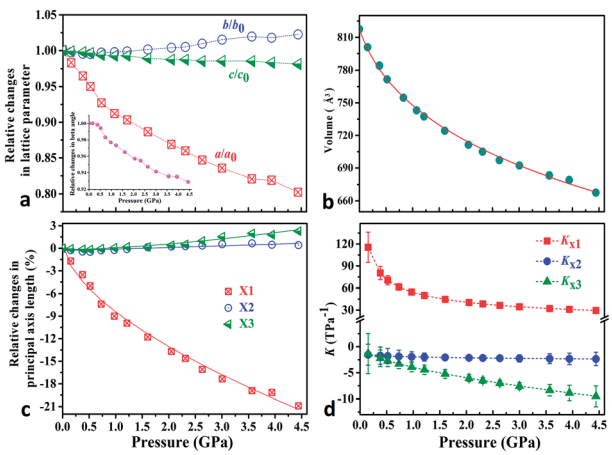


Fig. 2 (a) Relative changes of lattice parameters as a function of pressure; the beta angle changes are shown as an inset in (a). (b) The third order Birch–Murnaghan EoS fits[31] for cell volume *vs.* pressure (Fig. S3†). (c) Pressure-dependent relative changes in length for the three principal axes and (d) the corresponding principal compressibility $K_{X1}$, $K_{X2}$ and $K_{X3}$.

strain eigenvectors are not exactly along the crystallographic axes. To more clearly investigate the anomalous expansion of $Zn(CH_3COO)_2\cdot 2H_2O$, the principal compressibilities converted from variable-pressure lattice parameters are calculated using PASCal software[30] and the results are summarized in Table S2.† The relative changes for the principal axes and the corresponding principal compressibilities as a function of pressure are plotted in Fig. 2c and d (Tables S2 and S3†), where $K_{X1} = 40.4(15)$, $K_{X2} = -2.1(4)$, and $K_{X3} = -6.0(7)$ $TPa^{-1}$. Strikingly, the compressibility is negative along the (*X*2, *X*3)-plane, with the magnitude of $K_{(X2,\ X3)} = K_{X2} + K_{X3} = -8.1(8)$ $TPa^{-1}$. The (*X*2, *X*3)-plane with NAC behavior expands approximately within the (*b*, *c*)-plane located in an individual layer of the structure and the *X*1 principal axis is approximately parallel to the layer-stacking direction [100] (Fig. 1a and Table S2†). As summarized in Table 1, $Zn(CH_3COO)_2\cdot 2H_2O$ ranks the third among all hitherto known 8 NAC materials, and ranks the first if excluding those with phase transitions and metastable high-pressure NAC. Specifically, the NAC of $Zn(CH_3COO)_2\cdot 2H_2O$ is about an order of magnitude larger than that of the recently reported deep-UV nonlinear crystal $KBe_2BO_3F_2$ (KBBF),[22] and about 4.5 times larger than that of $NaV_2O_5$.[14] Though the NAC effect of the molecular framework Ag(tcm) (tcm = tricyanomethanide)[15] is similar to that of $Zn(CH_3COO)_2\cdot 2H_2O$, its phase transition at around 0.62 GPa would dramatically narrow down the applicable window to only about 1/7 that of $Zn(CH_3COO)_2\cdot 2H_2O$. In addition, under practical application circumstances, single-crystals or single-crystalline films with oriented NAC faces are required, and any pressure-induced phase transitions will inevitably lead to significant structural reconstruction and corresponding destruction of the crystal morphology (*e.g.* twinning induced cracking), hence being detrimental to the key NAC functionality. In this context, the non-emergence of a pressure-induced transition in compound $Zn(CH_3COO)_2\cdot 2H_2O$ is critically advantageous. Compared with 2-MeBzIm (2-methylbenzimidazole)[16] and $[Zn(L)_2(OH)_2]_n\cdot$guest (L = 4-(1*H*-naphtho[2,3-*d*]imidazole-1-yl)benzoate; the guest is water),[17] which exhibit stronger NAC effects but only in their metastable high-pressure phases, the ease of growing oriented single crystals and fabricating devices using complex $Zn(CH_3COO)_2\cdot 2H_2O$ and similar NAC materials under ambient conditions would be significantly more favorable as well.

In a second series of measurements, we collected the powder X-ray data of $Zn(CH_3COO)_2\cdot 2H_2O$ up to 7.53 GPa to check its phase stability at room temperature. Fig. S6† displays the raw two-dimensional X-ray diffraction images and diffraction peaks as a function of pressure. Below 4.28 GPa, the results are well consistent with previous measurements. However, further compression led to the disappearance of most sharp diffraction peaks and the prominent broadening of residual peaks, which indicates that the title compound loses its crystallinity. It is well-known that hybrid organic–inorganic compounds have low resistance to hydrostatic stress and amorphization often occurs at medium pressure (usually only a few GPa).[32,33] For example, the photovoltaic hybrid perovskite $(CH_3NH_3)PbI_3$ undergoes a gradual amorphization after the structural phase transformation takes place at 2.5 GPa.[34]

In order to elucidate the microscopic mechanism of the NAC behavior, the atomic geometries of the $Zn(CH_3COO)_2\cdot 2H_2O$ crystal were calculated, at intervals of about 0.5 GPa from ambient pressure to 4.44 GPa, using the first-principles geometry optimization based on the experimental lattice parameters.[35] The extracted NAC mechanism and details of structural evolution at ambient pressure, 2.05 and 4.44 GPa are shown in Fig. 3 and S7.† The variations of bond lengths and angles are shown in Fig. 4 and Table S4.† Owing to the relatively weak van der Waals interactions between adjacent layers, the supramolecular structure contracts considerably along the *a*-axis with increasing pressure. However, the *bc*-plane which is linked by stronger O–H···O bonds experiences fewer but unusual changes within the layer. The opposite rotating 'fan-shaped' unit, shown in Fig. 3, is utilized to schematically demonstrate the alterations of the coordination geometry and the corresponding NAC mechanism under pressure. The purple 'fan-shaped' unit represents the plane that includes Zn, C1, O3 and O2 of the acetate ligands, and water oxygen O1W within the half coordination geometry $[Zn(CH_3COO)\cdot(H_2O)]^+$, and the green 'fan-shaped' unit is comprised of counterpart atoms from the other half coordination geometry. Before we reveal the structural mechanism responsible for the NAC behavior, we need to stress the fact that two 'fan-shaped' $[Zn(CH_3COO)\cdot(H_2O)]^+$ units in each coordination geometry are confined by four $O1W^{vi}$–$H1^{vi}$···O2 and $O1W^{vii}$–$H2^{vii}$···O3 bonds approximately along the *b*- and *c*-axis in the layer, which allow the structure to respond uniquely to pressure. In the purple $[Zn(CH_3COO)\cdot(H_2O)]^+$ unit, the Zn–O2 and Zn–O1W bonds elongate and contract by about 8.6% and 1.3% from ambient pressure to 4.44 GPa, respectively. In addition, the $O1W^{vi}$–$H1^{vi}$···O2 bond shrinks by about 3.0% with

Table 1 Summary of the known NAC materials

| Materials | Pressure range (GPa) | NAC ($TPa^{-1}$) | Phase transition (*P*–*T*) |
|---|---|---|---|
| KBBF[22] | 0.22–6.39 | −1.0(2) | Non *P*–*T* |
| $NaV_2O_5$ (ref. 14) | 4–10 | −1.5 | Non *P*–*T* |
| Ag(tcm)[15] | 0–0.62 | −7.5(8) | Non *P*–*T* |
| 2-MeBzIm[16] | 0.24–2.40 | −15(6) | 0.22 GPa |
| $[Zn(L)_2(OH)_2]_n\cdot$guest[17] | 1.0–2.6 | −72(6) | 1.0, 2.6 GPa |
| $TlGaSe_2$ (ref. 23) | — | Indirect method | — |
| 2-(3′-Chlorophenyl) imidazoline[36] | 0.0001–0.08 | — | — |
| $Zn(CH_3COO)_2\cdot 2H_2O$ | 0.15–4.44 | −8.1(8) | Non *P*–*T* |

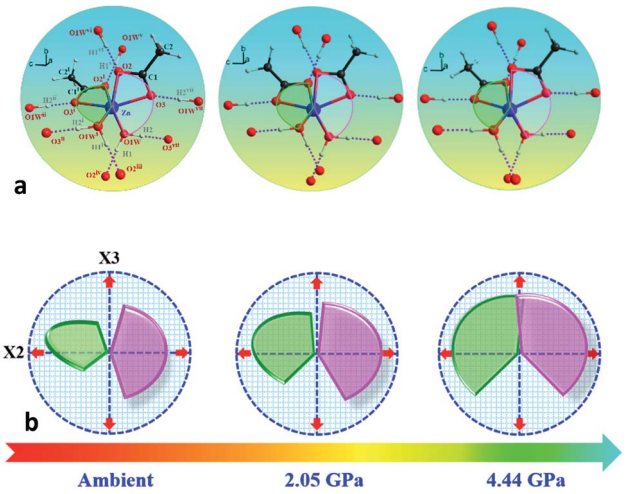


Fig. 3 (a) Schematic structural evolution mechanism responsible for the NAC behavior in $Zn(CH_3COO)_2\cdot 2H_2O$. Purple and green rotating 'fan-shaped' units represent the two half zinc coordination geometries in the crystal structure which lie approximately within planes through Zn, C1, O1W, O3, O2 and Zn, $C1^i$, $O1W^i$, $O3^i$, $O2^i$, respectively. (b) The generic mechanical response stimulating the expansion of *X*3 and *X*2 directions to the opposite rotation of the two 'fan-shaped' units under compression. The rotation and expansion of the 'fan-shaped' planes are exaggerated for illustrative purposes. Note: the *X*2 principal axis is approximately oppositely along the *c*-axis, and the *X*3 principal axis is oppositely along the *b*-axis (Table S2†). Atoms are colored as in Fig. 1. Symmetry codes: (i) $-x, y, 0.5 - z$; (ii) $x, -y, 0.5 + z$; (iii) $x, -1 + y, z$; (iv) $-x, -1 + y, 0.5 - z$; (v) $x, 1 + y, z$; (vi) $-x, 1 + y, 0.5 - z$; (vii) $-x, -y, -z$.

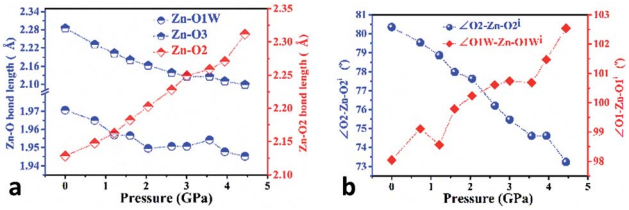


Fig. 4 Variation of selected bond lengths (a) and angles (b) in the $Zn(CH_3COO)_2\cdot 2H_2O$ structure as a function of pressure, calculated from DFT structural optimisations based on experimental lattice parameters.

an angle decrease of about 1.4% up to 4.44 GPa. Meanwhile, the intersectional angle O2–Zn–$O2^i$ of the two 'fan-shaped' units concurrently decreases from 80.35° to 73.24° (8.8%), accompanied by the increase of the O1W–Zn–$O1W^i$ angle from 98.05° to 102.54° (4.6%) as shown in Fig. 4 and S7.† The less significant contraction of the $O1W^{vi}$–$H1^{vi}\cdots$O2 distance and Zn–O1W bond is compensated for by the substantial increase of the Zn–O2 bond along the *b*-axis. And the dramatic closure of the angle between the two 'fan-shaped' structural units increases the elongated projection of the coordination geometry along the *b*-axis (*X*3 direction), hence leading to significant expansion of $K_{X3} = -6.0(7)$ $TPa^{-1}$. For understanding the expansion along *X*2 (approximately along the *c*-axis), we also need to take into account both the coordination bonding and hydrogen-bonding. The $O1W^{vii}$–$H2^{vii}\cdots$O3 bond length expands by about 0.4% with a bond angle decrease of about 0.2%, while the Zn–O3 bond length shrinks significantly by about 8.1%. Nevertheless, the slightly larger angle closure of the two 'fan-shaped' units can counterbalance the coupled contraction of the Zn–O3 and $O1W^{vii}$–$H2^{vii}\cdots$O3 bonds, which consequently leads to a small expansion along *X*2 with $K_{X2} = -2.1(4)$ $TPa^{-1}$. In addition, we need to take into account the synergistic contribution from the methyl group of the acetate ligand. During compression, it is forced to tilt and rotate along both *X*2 and *X*3 directions, hence facilitating the NAC (Fig. S7 and S8†). Such a complex cooperation process under pressure can be understood from the model cartoons in Fig. 3b and structural evolution in Fig. S7 and S8.†

Notably, though the NAC mechanism in $Zn(CH_3COO)_2\cdot 2H_2O$ is broadly reminiscent of the 'Lifshitz' scenario,[13,37] the cooperative involvement of coordination interactions, hydrogen-bonding and van der Waals forces in it extends beyond the singular molecular force in known materials. The underlying NAC mechanism in KBBF is primarily attributed to the flattening of the $Be_2BO_3F_2$ layer induced by the shrinkage of the Be–F bond under compression.[22] In molecular frameworks Ag(tcm)[15] and $[Zn(L)_2(OH)_2]_n\cdot$guest,[17] the NAC effects respectively arise from rippling of the honeycomb-like architecture and compression of flexible helices, which are both mainly caused by coordination bond flexing.

The above large NAC and compensating substantial shrinkage along the orthogonal axis in $Zn(CH_3COO)_2\cdot 2H_2O$ and similar materials could lead to many important technical applications under high-pressure working environments, such as precise pressure sensing materials.[38] A typical example is the pressure-converting material used in a Fabry–Perot interferometer pressure sensor, as schematically depicted in Fig. 5. To facilitate the discussion, we refer to the formula describing the refractive optical path difference (Δ) below:

$$\Delta = 2nh\cos\theta$$

where *n* is the refractive index, *h* is the thickness of the sensing crystal used in the interferometer, and $\theta$ is the angle of refraction. Upon compression from ambient pressure to 4.44 GPa, the *bc*-plane of the $Zn(CH_3COO)_2\cdot 2H_2O$ crystal expands by ~0.4%, which is unlikely to induce any significant changes in refractive index *n*. However, the *a*-axis of the crystal significantly decreases by ~20% in order to compensate for the expansion of the *bc*-

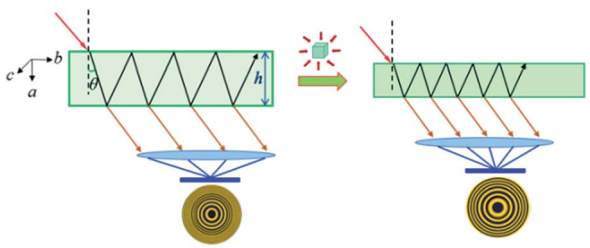


Fig. 5 Proposed schematic illustration of using $Zn(CH_3COO)_2\cdot 2H_2O$ crystals as a sensing medium in a Fabry–Perot interferometer pressure sensor by taking advantage of its large NAC.

plane, which consequently results in substantially proportional shrinkage of $h$. Therefore, the corresponding refractive optical path change $\Delta$ becomes very large under high-pressure conditions,[38] which dramatically enhances the shift of the diffracting fringes. In other words, the sensitivity of the Fabry–Perot interferometer could be significantly improved by using NAC crystals instead of a conventional sensing crystalline medium with positive compressibilities along all directions.

# Conclusions

In summary, we have revealed that a 2D molecular material, $Zn(CH_3COO)_2\cdot 2H_2O$, shows the extremely rare NAC effect over a wide pressure range *via* a combined approach of high-pressure experiments and first-principles calculations. Compared with other known NAC materials, $Zn(CH_3COO)_2\cdot 2H_2O$ exhibits a synergistic NAC mechanism which arises from a complex cooperation of in-plane coordination and hydrogen-bonding, and out-of-plane van der Waals interactions in its supramolecular structure. Moreover, we propose that $Zn(CH_3COO)_2\cdot 2H_2O$ and other NAC crystals could have important applications as pressure-converting materials for fabricating ultrasensitive pressure sensors. Considering the intrinsic electronic difference between hydrogen-bonding and other bonding forces, 2D materials assembled *via* hydrogen-bonding will offer a new materials platform for exploring pressure stimuli in quantum confined solids. More broadly, we envisage that the rich structural diversity in coordination compounds and other molecular materials in extreme environments will undoubtedly facilitate the discovery of new electronic, optical and magnetic functionalities from hybrid 2D materials by considering hydrogen-bonding and other supramolecular interactions.

# Experimental

### General information and synthesis

All chemicals and solvents were of reagent grade and used as received. Zinc salt $Zn(CH_3COO)_2\cdot 2H_2O$ was synthesized according to a literature method.[26]

### High-pressure synchrotron powder X-ray diffraction measurements (HP-PXRD)

The high-pressure synchrotron powder XRD experiments were performed at the 4W2 beamline of the Beijing Synchrotron Radiation Facility (BSRF). An X-ray beam with a wavelength of 0.6199 Å was focused on a $36 \times 12\ \mu m^2$ spot using Kirkpatrick–Baez mirrors. The hydrostatic pressure was exerted by the systematic diamond anvil cells (DACs) with a culet diameter of 400 μm. The samples in well ground powder form were placed in a hole of about 120 μm diameter in a pre-indented stainless steel gasket with a thickness of about 40 μm. Silicone oil served as the pressure-transmitting medium and ruby chips were placed for pressure calibration by measuring the fluorescence shift as a function of pressure.[39] The diffraction patterns were collected using a Pilatus 2M detector and integrated *via* the Fit2d suite of programs.[40] The cell parameters under different pressures were refined by the Pawley method using the whole profile fitting program implemented in Materials Studio.

### First-principles calculations

The first-principles calculations were performed by using CASTEP,[41,42] a total energy package based on plane-wave pseudopotential density functional theory (DFT).[41] The local density approximation (LDA)[43,44] was adopted to describe the exchange–correlation energy. Optimized ultrasoft pseudopotentials were adopted.[45] A kinetic energy cutoff of 500 eV and a Monkhorst–Pack $k$-point mesh of $6 \times 6 \times 2$ spanning less than 0.04 $Å^{-1}$ were chosen.[46] The atomic positions at intervals of about 0.5 GPa in the 0–4.44 GPa range were calculated by first-principles geometry optimization. In this geometry optimization, the cell parameters were fixed at the experimental values, and only the atomic positions at each pressure were optimized.

### Atomic force microscopy (AFM)

The surface topographies and the corresponding height profiles of different thickness nanosheets were collected using a Digital Instrument Multimode SPM in the tapping mode with a BRUKER RTESPA-300 tip. The bulk crystals were ground gently, and the nanosheets were prepared by dispersing the ground $Zn(CH_3COO)_2\cdot 2H_2O$ powder in ethanol and sonicating it for about 30 min in a KQ3200DE ultrasonic cleaner. Then the milky suspension in the vial was centrifuged at a rate of 4000 rpm. After keeping the tube still for a few minutes, the top suspension containing exfoliated nanosheets was deposited on a clean silicon substrate ($1 \times 1\ cm^2$). After the solvent on the substrate was evaporated completely, the as-prepared nanosheets were scanned at a rate of 1.00 Hz. The images were taken with a resolution of $256 \times 256$ pixels.[2]

### Transmission electron microscopy (TEM)

The bulk crystals were ground gently and dispersed in ethanol, and then the resulting suspension was deposited on a holey carbon support film prior to TEM testing. A Titan 60-300 Cs corrected transmission electron microscope operating at 300 kV was used to capture the bright-field images on the high dynamic range image plates. The nanosheets were very sensitive to the electron beam and lost their crystallinity within 5 s.

### Nanoindentation

The nanoindentation experiments were performed on the (100) and (001) facets using a nanoindenter (Triboindenter from Hysitron, Minneapolis, USA) with *in situ* imaging capability.[47] The machine continuously monitors and records the load ($P$) and displacement ($h$) of the indenter with force and displacement resolutions of 1 mN and 0.2 nm, respectively. A three-sided pyramidal Berkovich diamond indenter with a sharp tip radius of about 50 nm was used to indent the crystals. A standard fused silica sample with a reduced modulus of 72 GPa and hardness of 9 GPa was adopted for calibration. The raw data were analysed using the Oliver and Pharr method.[48,49]

## Conflicts of interest

There are no conflicts to declare.

## Acknowledgements

All authors are grateful for the funding support from the National Natural Science Foundation of China (Grant No. 21571072 and No. 11474292) and the support from the 4W2 beam line of Beijing Synchrotron Radiation Facility (BSRF). G. F. acknowledges the funding support from the Science Research Project of Hubei Provincial Department of Education, China (Grant No. B2018198).

## Notes and references

1 R. H. Baughman, S. Stafström, C. Cui and S. O. Dantas, *Science*, 1998, **279**, 1522–1524.
2 X. X. Jiang, Y. Yang, M. S. Molokeev, P. F. Gong, F. Liang, S. H. Wang, L. Liu, X. Wu, X. D. Li, Y. C. Li, S. F. Wu, W. Li, Y. C. Wu and Z. S. Lin, *Adv. Mater.*, 2018, **30**, 1801313.
3 A. L. Goodwin, D. A. Keen and M. G. Tucker, *Proc. Natl. Acad. Sci. U. S. A.*, 2008, **105**, 18708–18713.
4 A. B. Cairns, A. L. Thompson, M. G. Tucker, J. Haines and A. L. Goodwin, *J. Am. Chem. Soc.*, 2011, **134**, 4454–4456.
5 A. B. Cairns, J. Catafesta, C. Levelut, J. Rouquette, A. van der Lee, L. Peters, A. L. Thompson, V. Dmitriev, J. Haines and A. L. Goodwin, *Nat. Mater.*, 2013, **12**, 212–216.
6 H. J. Shepherd, T. Palamarciuc, P. Rosa, P. Guionneau, G. Molnár, J.-F. Létard and A. Bousseksou, *Angew. Chem., Int. Ed.*, 2012, **51**, 3910–3914.
7 C. H. Woodall, C. M. Beavers, J. Christensen, L. E. Hatcher, M. Intissar, A. Parlett, S. J. Teat, C. Reber and P. R. Raithby, *Angew. Chem., Int. Ed.*, 2013, **52**, 1–5.
8 W. Li, M. R. Probert, M. Kosa, T. D. Bennett, A. Thirumurugan, R. P. Burwood, M. Parinello, J. A. K. Howard and A. K. Cheetham, *J. Am. Chem. Soc.*, 2012, **134**, 11940–11943.
9 W. Cai and A. Katrusiak, *Nat. Commun.*, 2014, **5**, 4337.
10 Q. Zeng, K. Wang and B. Zou, *J. Am. Chem. Soc.*, 2017, **139**, 15648–15651.
11 A. D. Fortes, E. Suard and K. S. Knight, *Science*, 2011, **331**, 742–746.
12 W. Cai, J. He, W. Li and A. Katrusiak, *J. Mater. Chem. C*, 2014, **2**, 6471–6476.
13 A. B. Cairns and A. L. Goodwin, *Phys. Chem. Chem. Phys.*, 2015, **17**, 20449–20465.
14 I. Loa, K. Syassen, R. K. Kremer, U. Schwarz and M. Hanfland, *Phys. Rev. B*, 1999, **60**, R6945–R6948.
15 S. A. Hodgson, J. Adamson, S. J. Hunt, M. J. Cliffe, A. B. Cairns, A. L. Thompson, M. G. Tucker, N. P. Funnell and A. L. Goodwin, *Chem. Commun.*, 2014, **50**, 5264–5266.
16 W. Zieliński and A. Katrusiak, *Cryst. Growth Des.*, 2014, **14**, 4247–4253.
17 W. Cai, A. Gładysiak, M. Anioła, V. J. Smith, L. J. Barbour and A. Katrusiak, *J. Am. Chem. Soc.*, 2015, **137**, 9296–9301.
18 S. M. Clark, K.-J. Jeon, J.-Y. Chen and C.-S. Yoo, *Solid State Commun.*, 2013, **154**, 15–18.
19 A. P. Nayak, S. Bhattacharyya, J. Zhu, J. Liu, X. Wu, T. Pandey, C. Q. Jin, A. K. Singh, D. Akinwande and J.-F. Lin, *Nat. Commun.*, 2014, **5**, 3731.
20 T. Kmura, A. Asamitsu, Y. Tomioka and Y. Tokura, *Phys. Rev. Lett.*, 1997, **79**, 00319007.
21 P. Cervantes, Z. Slanic, F. Bridges, E. Knittle and Q. Williams, *J. Phys. Chem. Solids*, 2002, **63**(10), 1927–1933.
22 X. X. Jiang, S. Y. Luo, L. Kang, P. F. Gong, W. J. Yao, H. W. Huang, W. Li, R. J. Huang, W. Wang, Y. C. Li, X. D. Li, X. Wu, P. X. Lu, L. F. Li, C. T. Chen and Z. S. Lin, *Adv. Mater.*, 2015, **27**, 4851–4857.
23 M. Y. Seyidova and R. A. Suleymanov, *J. Appl. Phys.*, 2010, **108**, 063540.
24 A. M. Sweetman, S. P. Jarvis, H. Q. Sang, I. Lekkas, P. Rahe, Y. Wang, J. B. Wang, N. R. Champness, L. Kantorovich and P. Moriarty, *Nat. Commun.*, 2014, **5**, 3931.
25 G. A. Eby, *Med. Hypotheses*, 2010, **74**, 482–792.
26 T. Ishioka, A. Murata, Y. Kitagawa and K. T. Nakamura, *Acta Crystallogr.*, 1997, **C53**, 1029.
27 G. Q. Feng, D. Gui and W. Li, *Cryst. Growth Des.*, 2018, **18**, 4890–4895.
28 S. Varughese, M. S. R. N. Kiran, U. Ramamurty and G. R. Desiraju, *Angew. Chem., Int. Ed.*, 2013, **52**, 2701–2712.
29 D. Gui, L.-J. Ji, A. Muhammad, W. Li, W.-Z. Cai, Y.-C. Li, X.-D. Li, X. Wu and P.-X. Lu, *J. Phys. Chem. Lett.*, 2018, **9**(4), 751–755.
30 M. J. Cliffe and A. L. Goodwin, *J. Appl. Crystallogr.*, 2012, **45**, 1321–1329.
31 R. J. Angel, J. Gonzalez-Platas and M. Alvaro, *Z. Kristallogr.*, 2014, **229**, 405–419.
32 S. Sobczak and A. Katrusiak, *Cryst. Growth Des.*, 2018, **18**(2), 1082–1089.
33 Q. Li, S. Li, K. Wang, Z. W. Quan, Y. Meng and B. Zou, *J. Phys. Chem. Lett.*, 2017, **8**(2), 500–506.
34 M. Szafrański, A. Katrusiak and J. Phys, *Chem. Lett.*, 2016, **7**(17), 3458–3466.
35 G. Q. Feng, X. X. Jiang, W. J. Wei, P. F. Gong, L. Kang, Z. H. Li, Y. C. Li, X. D. Li, X. Wu, Z. S. Lin, W. Li and P. X. Lu, *Dalton Trans.*, 2016, **45**, 4303–4308.
36 M. Anioła, A. Katrusiak and R. Kia, *CrystEngComm*, 2012, **14**, 6424–6427.
37 I. M. Lifshitz, *Zh. Eksp. Teor. Fiz.*, 1952, **22**, 475–486.
38 R. H. Baughman, S. Stafstrom, C. X. Cui and S. O. Dantas, *Science*, 1998, **279**, 1522–1524.
39 H. K. Mao, J. Xu and P. M. Bell, *J. Geophys. Res.*, 1986, **91**, 4673–4676.
40 J. Hammersley, *Fit2d User Manual*, ESRF, Grenoble, France, 1996.
41 S. J. Clark, M. D. Segall, C. J. Pickard, P. J. Hasnip, M. J. Prob ert, K. M. Refson and C. Z. Payne, *Kristallografiya*, 2005, **220**, 567–570.
42 M. C. Payne, M. P. Teter, D. C. Allan, T. A. Arias and J. D. Joannopoulos, *Rev. Mod. Phys.*, 1992, **64**, 1045–1097.

 

43 J. P. Perdew and A. Zunger, *Phys. Rev. B: Condens. Matter*, 1981, **23**, 5079.
44 D. M. Ceperley and B. J. Alder, *Phys. Rev. Lett.*, 1980, **45**, 566–569.
45 A. M. Rappe, K. M. Rabe, E. Kaxiras and J. D. Joannopoulos, *Phys. Rev. B: Condens. Matter*, 1990, **41**(2), 1227.
46 H. J. Monkhorst and J. D. Pack, *Phys. Rev. B: Solid State*, 1976, **13**, 5188–5192.
47 L.-Y. Dong, S.-J. Sun, Z.-Y. Deng, W. Li, F.-X. Wei, Y.-J. Qi, Y.-C. Li, X.-D. Li, P.-X. Lu and U. Ramamurty, *Comput. Mater. Sci.*, 2018, **141**, 49.
48 W. C. Oliver and G. M. Pharr, *J. Mater. Res.*, 1992, **7**, 1564–1583.
49 W. C. Oliver and G. M. Pharr, *J. Mater. Res.*, 2004, **19**, 3–20.